Post-contact droplet spreading and bubble entrapment on a smooth surface

Lige Zhang, Tejaswi Soori, Arif Rokoni, and Ying Sun*
Department of Mechanical Engineering and Mechanics
Drexel University, Philadelphia, PA 19104, USA

Abstract

In this paper, we use a combination of high-speed imaging and total internal reflection microscopy (TIRM) to study post-contact spreading dynamics and bubble entrapment of droplets impacting on surfaces lubricated with an immiscible fluid, following dimple and film modes of contact. The post-contact droplet spreading entraps two types of bubbles: (a) surface and (b) bulk, where the former occurs when the bubbles remain at the droplet-surface interface and the latter takes place within the droplet because of the impact-induced air cavity closure. The dimple mode of droplet-surface contact shows an absence of central surface bubble due to the contact point at the drop center and the subsequent axisymmetric spreading. The surface radial bubbles can be suppressed by tuning the impact velocity, liquid surface tension, and viscosity. Early-stage post-contact spreading dynamics are then studied for the dimple mode, where a visco-capillary scaling for the spreading radius r_{wet} versus time t of $r_{wet} \sim t$ is observed. Finally, the critical capillary number for wetting failure scaling is used to predict the presence of surface radial bubble entrapment with good accuracy.

* Corresponding author. Tel.: +1(215)895-1373; E-mail: ys347@drexel.edu.

I. INTRODUCTION

The impact of a liquid droplet onto a surface is ubiquitous in natural and industrial processes. Bubble entrapment phenomena during post-contact spreading of the droplet can be advantageous as well as undesirable, depending on the application. Entrapment of bubbles can lead to poor quality of spray coating [1,2], inkjet printing [3,4], and pesticide application in agricultural fields [5,6], as well as reduced heat transfer performance in spray cooling [7]. Whereas bubbles entrapped during atomized fuel drops impacting the chambers of internal combustion engines [8] can aid in further atomization and enhance combustion. Moreover, the entrapment of bubbles can provide important insights into the impact conditions and droplet trajectories in forensic sciences such as bloodstain pattern analysis [9,10].

Figure 1 shows the schematic of a liquid droplet of radius, R, impacting a dry surface at velocity, U_0. Prior to the droplet contacting the surface, the pressure within the air layer between the droplet and surface increases, causing a dimple at the droplet-air interface directly under the center of the droplet. For dry surfaces, the impacting droplet bounces off from the surface at low impact velocities and contacts the surface via the film mode at high impact velocities, where the contact is initiated at the thinnest region of the extended interstitial air film. Inset in Fig. 1 shows the contact line geometry during post-contact spreading, where $\lambda = \mu_{\mathrm{g}}/\mu_{\mathrm{l}}$ is the gas to liquid viscosity ratio, θ_{mic} is the intrinsic microscopic contact angle, taken as the static contact angle at the three-phase contact line [11], and U_{wet} is the contact line speed.

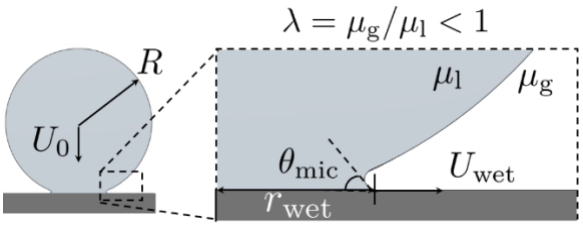

FIG. 1. Schematic of a droplet with radius, R, impacting on a dry surface at velocity of U_0. Inset shows the contact line geometry during post-contact spreading. Here, $\lambda = \mu_g/\mu_l$ is the gas to liquid viscosity ratio, θ_{mic} is the intrinsic microscopic contact angle, r_{wet} and U_{wet} are the wetting radius and contact line speed, respectively.

The post-contact bubble entrapment phenomena have been widely studied for droplet impact on dry surfaces, where two key scenarios are reported: surface and bulk bubbles. The surface bubbles are the ones that are entrapped on the surface and are often observed for hydrophilic and hydrophobic surfaces [12–16], while the bulk bubbles are those trapped within the droplet and are reported on superhydrophobic surfaces [16]. The bulk bubble occurs as a central bubble, resulted from the closure of an air cavity caused by the impact induced capillary waves traveling over the droplet's top surface [16–19]. While the bulk bubbles eventually escape from the droplet due to buoyancy, the surface bubbles which are generally $\mathcal{O}(10^0 - 10^2)$μm in diameter [13,20,21] remain entrapped at the surface in the form of central and radial bubbles [13,16,20,22–24]. These surface bubbles are detrimental and can lead to poor quality of spray coating and inkjet printing. Hence, we limit our discussions to surface central and radial bubbles only and hereinafter call the entrapment scenarios as central and radial bubbles, respectively.

Once the droplet contacts the dry surface at the thinnest region of the air film away from the central dimple, also called the film mode, an air disc is entrapped under the droplet's center and the inward moving contact line causes the entrapped air disc to evolve into a central bubble [21,25,26]. However, the topological events that lead to the entrapment of radial bubbles are rather contentious, where some researchers [25,27] claim that the random contacts between the

levitated lamella and the surface ahead of the outward moving contact line cause the entrapment of radial bubbles, while others [28,29] claim that the cusps observed on the outward moving contact line cause the radial bubbles. The cusps mentioned here refers to the sawtooth-type [20] contact line instability reported in coating studies. The two above arguments are more applicable to large impact Weber number cases ($\mathrm{We} = \rho_l {U_0}^2 R/\gamma \gg 1$) where the precursor lamella must exist *a priori* [25,28,29], ahead of the contact line. Here, ρ_l and γ are the liquid density and liquid-air surface tension, respectively. In contrast, studies of the corresponding bubble entrapment topological events for droplets impacting at low and moderate impact velocities ($\mathrm{We} \sim \mathcal{O}(10^0 - 10^1)$) are lacking.

Drop impact on wet surfaces, depending on the liquid thickness, h_f, can be broadly classified into the scenarios of (a) thin films ($h_f \leq R$) [20,21,26,30–34] and (b) liquid pools ($h_f > R$) [35–44]. For bubble entrapment during droplet impact on liquid pools, both miscible [35,37,38,40–43] and immiscible [36,39,44] cases have been studied and a variety of bubble entrapment morphologies such as crater collapse induced entrapment in immiscible pools [36,43], as well as air disc splitting [37,38] and microbubble entrapments [35,42,44] in miscible pools, have been reported. For thin liquid film surfaces ($h_f \leq R$), bubble entrapment studies have been rather limited to large impact velocities and to cases where both droplet and thin film are of the same fluid [20,21,26].

To address this gap, in the present study, we investigate the bubble entrapment during impact on thin films where the droplet and thin film are immiscible with each other. The results presented herein show that, similar to dry surfaces, drops with large impact velocities on immiscible thin films lead to the film mode of contact with the entrapment of central and radial bubbles. For low impact velocities, the droplet undergoes dimple contact mode, where the contact and subsequent

spreading are axisymmetric, which leads to suppression of surface central bubbles and only the bulk central and surface radial bubbles are entrapped. Figure 2(a) shows the schematic of the contact modes on a lubricated surface. Figure 2(b) depicts the post-contact dynamics and consequent bubble entrapment for the film contact. Figure 2(c) is the pre-contact and Fig. 2(d) the post-contact and subsequent bubble entrapment for dimple mode of contact. In Figs. 2(b)-(d), time $t = 0$ is set at the instance of droplet-surface contact, represented by the red downward arrows. In the post-contact dynamics of film and dimple modes, the dash-dotted lines represent the axisymmetric line of an impacting drop, and the blue arrows represent the liquid spreading direction after contact.

Bulk and surface bubbles are observed for drop impact on lubricated surfaces, as demonstrated in Figs. 2(b) and (d). The bulk bubble (also known as the "detached bubble") entrapment is due to the air cavity closure [45,46]. The above-mentioned air cavity is a result of the capillary waves traveling over the droplet's top surface which eventually converge at the droplet's apex, illustrated in the pre-contact dynamic of Fig. 2(c). The surface bubbles (also known as "attached bubbles") entrapment is due to the post-contact triple line movement. The radially inward moving triple line entraps the central surface bubble [22,47], and the radially outward moving triple line entraps the radial surface bubbles due to contact line sawtooth instability [48].

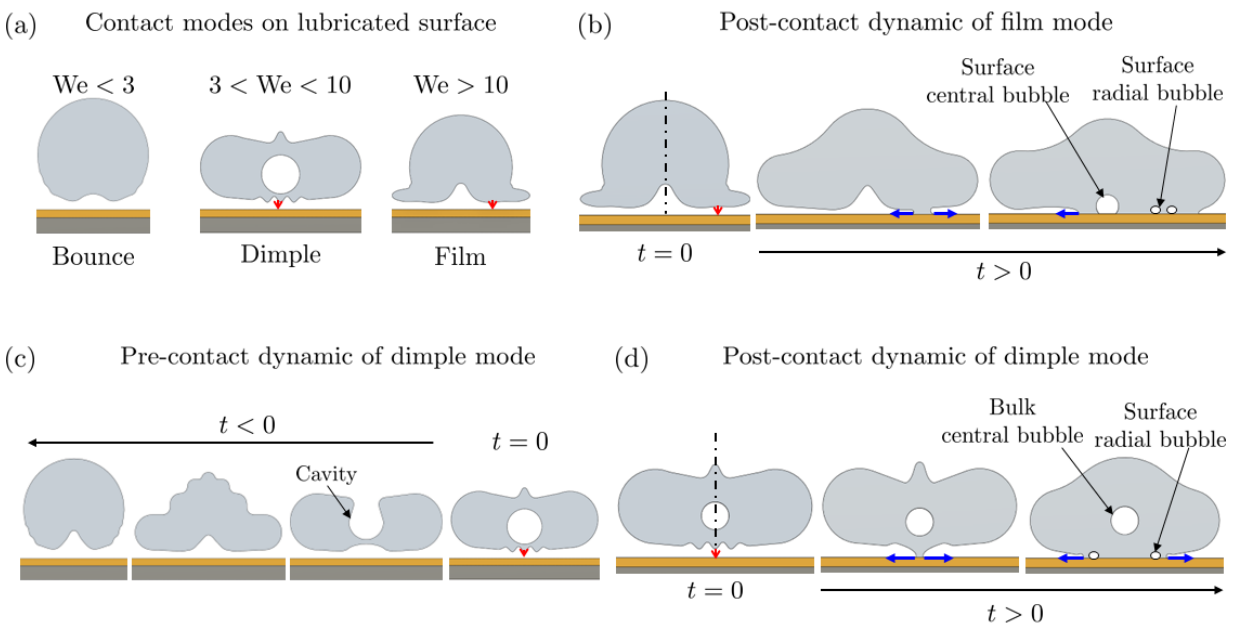

FIG. 2 (a) shows the bouncing, dimple, and film modes of contact on a lubricated surface, depending on the impact Weber number, $\mathrm{We} = \frac{\rho U_0^2 R}{\gamma}$. The red downward arrows indicate the contact locations at the center of the air film and outside of the dimple region for dimple and film modes of contact, respectively. (b) shows the schematic of the post-contact dynamic of film mode, entrapping a surface central bubble and surface radial bubbles. (c) is the schematic of the pre-contact dynamic of dimple mode, taken from Zhang et al. [34]. A central cavity induced by capillary wave encloses into a bulk central bubble, which perturbs the air film at the dimple region. The unstable wave due to the perturbation results in the dimple contact. (d) shows the schematic of the post-contact dynamic of dimple mode, entrapping a bulk central bubble and surface radial bubbles. In (b)-(d), time $\mathrm{t} = 0$ is set at the instance of droplet-surface contact. In (b) and (d), the dash-dotted lines represent the axisymmetric line of an impacting drop, and the blue arrows represent the liquid spreading direction after contact.

To suppress the entrapment of surface bubbles during post-contact droplet spreading, a detailed understanding of the dynamics and failure mechanisms of the contact line motion is crucial. Note that the term 'contact line' corresponds to the 'triple line' between the droplet, air, and the lubricated oil film, which is assumed to have negligible deformation during the time scale of the post-contact spreading. Given that the droplet impact and spreading occur over a short time frame ($\sim \mathcal{O}(10^0 \mathrm{ms})$) [20,21,26,49,50] and the bubble entrapment happens within the first several

hundred microseconds [12,13,20,21,26], it is important to consider the early-stage [51] spreading when the spreading radius, r_{wet}, is less than the droplet radius, R. The early-stage spreading can be classified into the kinematic phase, where the dimensionless spreading radius following $r^* \sim t^{*0.5}$ and the spreading phase, where $r^* \sim \mathrm{f}(\mathrm{We}, \mathrm{Re}, \theta_{\mathrm{mic}}, t^*, \ldots)$ is a function of the impact conditions and liquid properties, where $\mathrm{Re} = \rho_{\mathrm{l}} U_0 R/\mu_{\mathrm{l}}$ is the Reynolds number [49,50]. Here, $r^* = r_{\mathrm{max}}/R$, with r_{max} being the instantaneous maximum radial extent of the droplet measured using side-view images, and $t^* = tU_0/R$ is the dimensionless time. Note that, in the above spreading laws [49–51], the spreading radius based on side-view visualizations can only provide the maximum radial extent of the droplet not the actual contact line location underneath the droplet due to the inability of visualizing the nanometer-thick air layer ahead of the contact line. Bottom-view visualization can overcome this challenge but has not been applied to investigate early-stage spreading dynamics of free-falling droplets on surfaces.

Instead, early-stage pendant drops spreading on surfaces and coalescence of two droplets have been studied using a combination of side-view and bottom-view imaging, as well as x-ray visualization and electrical methods [52,53,62–66,54–61]. The early-stage coalescence of two droplets is analogous to pendant drop spreading, where the symmetry plane of the two coalescing droplets is equivalent to the spreading surface [52,58]. At early times, coalescing droplets have been shown to follow a visco-capillary scaling of $r_{\mathrm{wet}}/R \sim t/\tau_{\mathrm{VC}}$, where r_{wet} is the wetted radius of the liquid and $\tau_{\mathrm{VC}} \equiv \mu_{\mathrm{l}} R/\gamma$ the visco-capillary time scale [53,58–66], followed by an inertio-capillary scaling of $r_{\mathrm{wet}}/R \sim (t/\tau_{\mathrm{IC}})^{\alpha}$, where $\alpha \approx 0.5$ and $\tau_{\mathrm{IC}} \equiv \sqrt{\rho_{\mathrm{l}} R^3/\gamma}$ is the inertio-capillary timescale [52–60]. Variations in α have also been reported for pendant drops spreading, depending on whether the droplet wets the surface perfectly ($\alpha = 0.5$) or partially ($\alpha < 0.5$) [52–58]. The above mentioned inertio-capillary and visco-capillary spreading laws consider droplets with

spherical geometry. However, during droplet impact at We $> \mathcal{O}(10^0)$, the bottom of the droplet deforms due to inertial effects and the role of the interstitial air film in the early-stage spreading dynamics is unclear.

In this paper, we present the experimental evidence of surface bubble suppression during post-impact contact line motion for droplets undergoing dimple mode of droplet-surface contact, where an axisymmetric contact is initiated at the central axis of the droplet's bottom. The impact velocity and liquid properties are varied to study their effects on the bubble entrapment scenarios. The pre-contact air film and post-failure contact line dynamics are both visualized using the total internal reflection microscopy [67,68] (TIRM) which can probe the air film of thickness $\sim \mathcal{O}(10^0 - 10^2)$ nm. The early-stage post-contact spreading dynamics for the dimple contact mode is measured and the result is compared against existing spreading laws for pendant drop spreading and drop coalescence scenarios. The critical capillary number for bubble entrapment of various fluids is then estimated based on the water droplet case, utilizing the critical capillary number for wetting failure scaling.

II. EXPERIMENTS

Total internal reflection microscopy has been used to visualize the pre-contact air film morphology and failure modes upon droplet impact [33,34,67,69]. The TIRM technique enables the thickness measurement of $\sim \mathcal{O}(10^0 - 10^2)$ nm [33,34,67–69] for an interstitial air film underneath a droplet and allows for the accurate identification of contact positions [33,34]. In our experiments, the high-speed TIRM was also adopted to visualize the post-impact contact line motion and bubble entrapment. A synchronized side-view high speed camera, illuminated by an LED light source, was used to capture the droplet's in-flight radius R and impact velocity U_0.

Water, methanol, and methanol-water mixture droplets were used to study the effect of surface tension on spreading dynamics and bubble entrapment. Additionally, glycerol-water mixture droplets were also used to study the effect of viscosity on spreading dynamics and bubble entrapment. The physical properties of fluids used in our experiments are tabulated in Table I. The droplet radius was maintained in the range of $0.61 < R < 1.10$ mm and the impact velocity were maintained in the range $0.4 < U_0 < 0.9$ m/s by changing the drop dispensing height. The impact We was maintained between 3 and 10 to obtain the axisymmetric droplet-surface contact at the droplet's central axis, which is called the dimple contact mode [34].

Table I. Physical properties of fluids at 25 ℃ used in our experiments

Fluids	Density ρ_l (kg m^{-3})	Viscosity μ_l (Pa s)	Surface tension γ (N m^{-1})	Refractive index n
DI water	997	10^{-3}	0.072	1.33
Methanol (MeOH)	791.7	0.5×10^{-3}	0.023	1.326
4.04 wt% methanol-water solution	991.5	$\approx 10^{-3}$	0.066	1.335
80.22 wt% methanol-water solution	846.3	$\approx 10^{-3}$	0.026	1.337
40 wt% glycerol-water solution	1097	3.7×10^{-3}	0.07	1.38
Silicone oil [70] (film)	977	97.7	0.021	1.40

To isolate the effect of substrate asperities on contact and spreading and to provide an optically transparent pathway for the TIRM measurement, lubricated substrates using silicone oil coated on glass slide were prepared for drop impact and spreading experiments. A thin silicone oil film of 5 μm was spin coated onto a glass slide at a rotational speed of 10,000 rpm for 25 min. The film thickness was measured by taking the weight difference before and after the spin-coating. The silicone oil viscosity and film thickness were chosen carefully to avoid early onset of air film rupture due to air-oil interface deformations [33]. The dimensionless oil film thickness $\delta =$

$h_{\text{oil}}/2R = 0.005$ was two orders of magnitude smaller than 0.7, the threshold for lubricant deformation, where h_{oil} is the oil film thickness [71]. An estimate for the maximum deformation of the lubricated film during droplet impact was also made using the empirical relation developed in Lakshman et al. [72], where the deformation amplitude scales as $A_0 \sim {h_{\text{oil}}}^2/\mu_{\text{oil}}$ and μ_{oil} is the silicone oil viscosity. For the silicone oil film thickness and viscosity used in this study, $A_0 \sim \mathcal{O}(10^{-13}\text{m})$, which suggests negligible deformation [34]. The lubricated substrate was placed on top of a dove prism with a refractive index of $n = 1.52$ and a p-polarized monochromatic light source of wavelength $\lambda_{\text{light}} = 660$ nm was used to illuminate the silicone oil-air interface at an incident angle of 49.9° for TIRM imaging. A Phantom high-speed camera captures the TIRM images in 16-bit format with a pixel resolution of 5 μm. The field of view and temporal resolution was adjusted between 336×336 and 512×512 pixels, and 25,000-46,000 frames per second, depending on total wetting region. The TIRM measurement was calibrated against the correction reported by Shirota et al. [68].

III. RESULTS AND DISCUSSION

In this section, we present the experimental results of central and radial bubble entrapment scenarios observed during droplet impact on a lubricated surface. In Sec. III. A, we discuss the results of central bubble entrapment during film and dimple modes of contact and show that the central bubble entrapment is absent for dimple contact mode. Radial bubble entrapment of the dimple mode as a function of the impact velocity and droplet liquid properties is then discussed in Sec. III. B. Further, we present the early-stage post-contact spreading dynamics for droplets undergoing axisymmetric dimple contact mode and compare the spreading rates with existing scaling laws. Finally, using the contact line velocity measured from the spreading speed, we

compare the experimentally determined capillary number with the critical capillary number above which contact line instability leads to bubble entrapment.

A. Central bubble entrapment

To study the effect of impact velocity and the resulting contact mode on the bubble entrapment scenarios, we varied the impact Weber number such that, for $3 < \mathrm{We} < 10$, the droplets contacted the surface via the axisymmetric dimple mode and, for $\mathrm{We} \approx 10.3$, the droplets exhibited non-axisymmetric film contact mode. Figure 3 shows the post-contact bubble entrapment scenarios observed for water droplets undergoing film and dimple contact modes. In Fig. 3 (a), TIRM images of post-contact spreading of a water droplet on a lubricated surface at $\mathrm{We} \approx 10.3$ are shown, where the second column shows a non-axisymmetric film contact initiation (marked by a red circle). Once the contact line advances, a central surface bubble is entrapped, as shown in the third column (marked by a blue circle). At later stages (fourth column) of spreading, several small radial microbubbles are also entrapped. A magnified view of both central and radial bubbles entrapped during spreading of a water droplet undergoing film mode is shown in the Supplemental Material [83]. The central and radial bubbles observed herein are similar to the bubble entrapment results reported in past studies [20,21,25,26] of droplet impacting miscible thin films, where the film contact mode was observed at large impact velocities. When the impact velocity was reduced, the dimple contact mode was observed, where the droplet-surface contact occurred via an axisymmetric contact at the droplet's central axis. In Fig. 3(b), TIRM views of post-contact spreading for a water droplet impacting at $\mathrm{We} \approx 4.4$ is shown, where the second column shows the axisymmetric contact initiation (marked in red circle). In columns three and four, the

entrapment of radial bubbles (marked in blue ellipse) is clearly visible. As seen from the TIRM views at time $t = 0$, the thickness of the air film underneath the droplet and ahead of the contact line for the film mode (Fig. 3(a)) is much smaller than the one seen for the dimple mode (Fig. 3(b)), where the former has low light intensity than the latter, suggesting smaller air film heights. Comparing the time instances ($t = 0$, 0.08, and 0.2 ms) in Figs. 3(a) and (b), we observe that the droplet spreading is slower for the dimple mode than the film mode, with the latter spreading radially with unequal speeds, whereas the former spreads almost uniformly. The central bubble observed for the film mode (Fig. 3(a)) is completely absent for the dimple mode (Fig. 3(b)) due to the axisymmetric spreading of the droplet on the lubricated surface. Moreover, all water droplets that exhibit the dimple mode of contact showed the absence of a central bubble. When the droplet spreads on the surface after the film contact, the air present within the dimple region is unable to drain within the duration of spreading, and thus entraps a central bubble. However, for the dimple mode, the axisymmetric contact and subsequent outward motion of the contact line, naturally avoids the central bubble entrapment. Similar dimple contact mode and central bubble suppression mechanisms were also obtained for droplets of methanol, as well as 4.04% and 80.22% methanol-water mixture droplets, and the detailed results are discussed in Sec. III. B. 2. However, 40% glycerol-water mixture drops did not exhibit contact and eventually bounced off, the details of which are also discussed in Sec. III. B. 2.

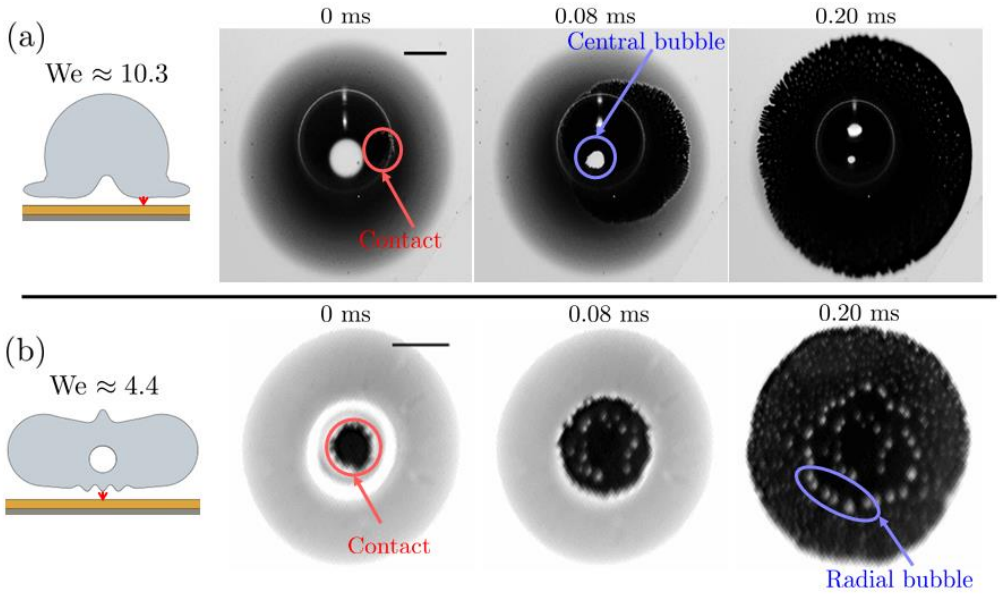

FIG. 3. TIRM images of water droplets exhibiting (a) film contact mode at We ≈ 10.3 and (b) dimple contact mode at We ≈ 4.4. Images are captured at contact ($t = 0$), and 0.08 and 0.2 ms after contact, respectively. The red circle indicates the contact location, and blue circle indicates the bubble entrapment location. A comparison of film and dimple mode post-contact TIRM images shows that the central bubble entrapped during film mode post-contact spreading but is completely absent for the dimple mode. Radial bubbles are entrapped for both contact modes. Scalebars represent 0.5 mm.

B. Radial bubble entrapment for dimple contact

1. Effect of impact velocity on radial bubble entrapment

To study the effect of impact velocity on radial bubble entrapment mechanism, we visualized the post-contact spreading of water droplets exhibiting dimple contact mode at different impact Weber numbers. Figure 4 shows the TIRM images of water droplets exhibiting dimple contact mode at two different We values. The time t is nondimensionalized with the visco-capillary timescale, $\tau_{VC} = \mu_l R/\gamma$. In Fig. 4(a) and (b), we show the water droplet impacting at We ≈ 4.4 and We ≈ 3.5, respectively, where the radial bubble entrapment observed for the higher We droplet is completely absent for lower We droplet. The right panels in top and bottom rows of Fig. 4 show that the water droplet with higher impact We reaches the maximum spreading radius within

$t/\tau_{VC} = 25.2$ while a similar water droplet with lower impact We requires $t/\tau_{VC} = 40.9$ to reach the maximum spreading radius. The result suggests that the droplet with higher impact velocity exhibits a faster contact line velocity leading to entrapment of radial bubbles. While both the droplets show suppression of central bubble entrapment, the water droplet impacting at We ≈ 3.5 shows suppression of all bubbles, confirming that the impact velocity can be tuned to achieve favorable droplet-surface spreading. In Sec. III. B. 4., we describe in detail the critical contact velocity and associated critical capillary number for bubble entrapment in case of methanol and its aqueous mixtures using the water droplet case at We ≈ 4.4 as the baseline threshold.

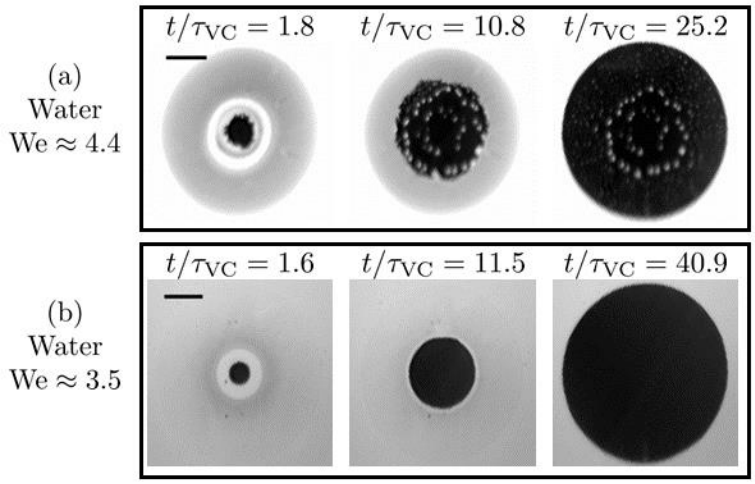

FIG. 4. TIRM images of water droplets exhibiting dimple contact mode at (a) We ≈ 4.4 and (b) We ≈ 3.5, respectively. The post-contact time values, t, are made dimensionless using the visco-capillary timescale, $\tau_{VC} = \mu_l R/\gamma$. The dimensionless times in (a) are $t/\tau_{VC} = 1.8$, 10.8 and 25.2 and in (b) are $t/\tau_{VC} = 1.6$, 11.5 and 40.9. The visco-capillary timescale for (a) We ≈ 4.4 and (b) We ≈ 3.5 are $\tau_{VC} = 13$ μs and $\tau_{VC} = 14$ μs, respectively. As the impact velocity (or impact We) is reduced from 4.4 (a) to 3.5 (b), the entrapped radial bubbles are completely suppressed. Scalebars represent 0.5 mm.

2. Effect of droplet properties on radial bubble entrapment

The effect of liquid properties on radial bubble entrapment was studied by using droplets of water, methanol-water mixtures, methanol, and glycerol-water mixture, where the water,

methanol-water mixtures, and methanol droplets had similar viscosity values and water and glycerol-water mixture droplets had similar surface tension values. In Fig. 5, the TIRM images of post-contact spreading dynamics are shown for (a) water, (b) 80.22% methanol-water mixture, (c) methanol, and (d) 40% glycerol-water mixture droplets, respectively. While the dimensionless time $t/\tau_{VC} = 0$ in Figs. 5(a)-(c) correspond to the instant when the droplet-surface contact is initiated via the dimple mode, in Fig. 5(d) it corresponds to the instant when the air film thickness reaches an absolute minimum. Figures 5(a)-(c) show the post-contact spreading dynamics and bubble entrapment scenarios for liquids with similar viscosity but different surface tension values, with 4.04% methanol-water mixture droplets (not shown here) also showing similar results. The air film profiles ahead of wetting front for the cases shown in Fig. 5(a)-(c) are demonstrated in Section S.5 of the Supplemental Materials [83]. As seen from the TIRM middle panels of water (Fig. 5(a)), 80.22% methanol-water mixture (Fig. 5(b)), and methanol (Fig. 5(c)) droplets, where the dimensionless times are $t/\tau_{VC} = 10.8$, 10, and 10.2, respectively, the water droplet has entrapped significant number of radial bubbles, while the 80.22% methanol-water mixture droplet has entrapped very few radial bubbles, and the methanol droplet has entrapped no radial bubbles. Moreover, TIRM views at dimensionless times $t/\tau_{VC} = 25.2$ and 25.4 in Figs. 5(a) and (b), and (c), respectively, show that the number of bubbles entrapped post-spreading is significantly reduced when the liquid surface tension is decreased, with methanol droplet at t/τ_{VC} =25 showing the absence of all surface bubbles. Figures 5(a) and (d) show the post-contact spreading dynamics and bubble entrapment scenarios for liquids with similar surface tension but different viscosity values, although the glycerol-water mixture droplet shown in Fig. 5(d) does not exhibit contact and instead bounces off. The glycerol-water mixture droplets did not exhibit dimple contact mode due to a stable air layer between the droplet and lubricated surface. The air layer is stable due to

the higher viscosity of the droplet resulting in faster attenuation of the impact induced capillary waves of wavelength $\lambda_c = \gamma/\rho_l U_0^2$, with the attenuation coefficient $\beta = \mu_l\sqrt{\frac{128\pi^3}{9\rho_l\gamma\lambda_c}}$, and therefore the air cavity formation and subsequent dimple contact mode are suppressed [34]. The dimensionless times for the 40% glycerol-water mixture droplet show that once the droplet reaches a minimum height, the droplet glides over the lubricated surface over an extended period prior to bouncing, which is similar to the results reported in previous studies on viscous droplet impacting dry surfaces and lubricated films [33,34,67,69,73–76]. The critical capillary number for bubble entrapment in case of methanol and its aqueous solutions are estimated using the threshold capillary number for water droplet at We ≈ 4.4, the details of which are explained in Sec. III. B. 4.

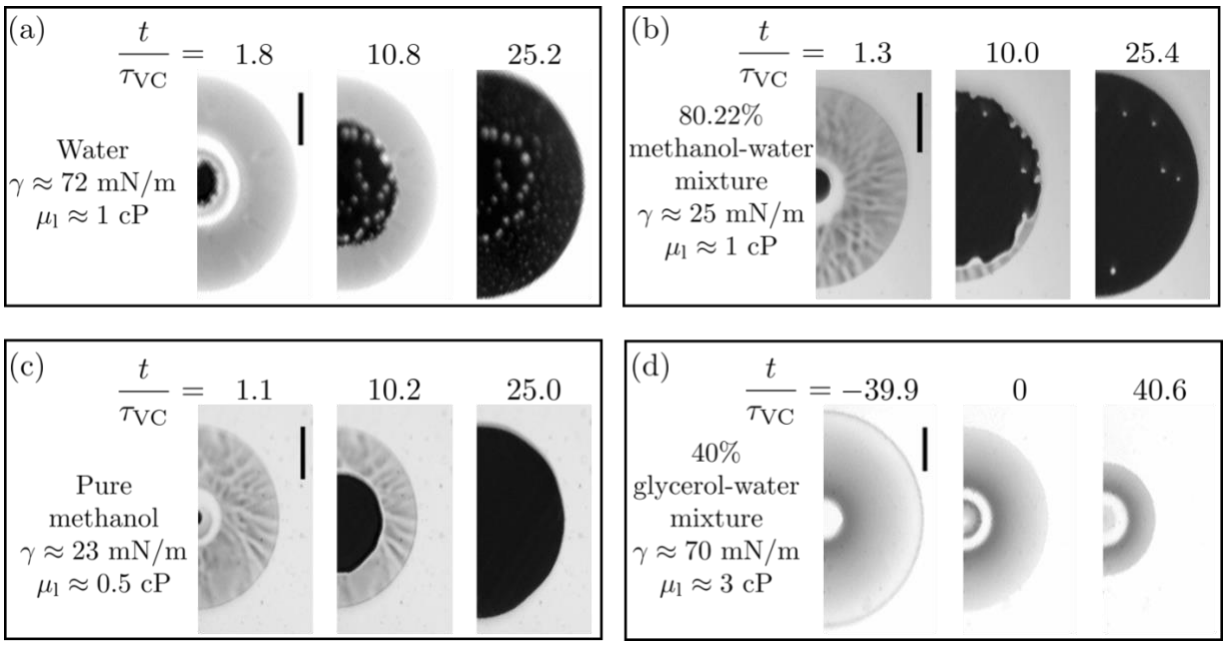

FIG. 5. TIRM images of (a) water droplet impacting at We ≈ 4.4, (b) 80.22% methanol-water mixture droplet impacting at We ≈ 6.5, (c) methanol droplet impacting at We ≈5.4, and (d) 40% glycerol-water mixture droplet impacting at We ≈ 3.7. While the droplets in (a)-(c) exhibited dimple contact mode, the droplet in (d) bounced off without contacting the surface due to higher droplet viscosity suppressing the thin film instability necessary for the dimple contact mode. When

the droplet surface tension was reduced from 72 mN/m in (a) to 25 mN/m in (b), the size of the entrapped radial bubbles reduced and for 23 mN/m in (c), all bubbles were suppressed. The dimensionless time $t/\tau_{\mathrm{VC}} = 0$ in (a)-(c) corresponds to the time at droplet-surface contact. In (d), the dimensionless time $t/\tau_{\mathrm{VC}} = 0$ corresponds to the instance when the air film reaches the minimum height. Scalebars represent 0.5 mm.

3. Early-stage spreading dynamics

To study the contact line speed during post-contact spreading and its effects on radial bubble entrapment, the TIRM views of the dimple mode droplets were used to extract spreading radius r_{wet} over the entire spreading duration. The spreading radius $r_{\mathrm{wet}}(t)$ was nondimensionalized using the droplet radius R and the time t was nondimensionalized using the visco-capillary timescale, $\tau_{\mathrm{VC}} = \mu_{\mathrm{l}} R/\gamma$, for all droplets undergoing dimple mode spreading. Figure 6(a) shows the synchronized side-view and TIRM images of dimple mode spreading behavior for 80.22% methanol-water mixture at dimensionless times $t/\tau_{\mathrm{VC}} = 1.36$, 6.8, and 14.97. Figure 6(b) shows a log-log plot of the dimensionless spreading radius r_{wet}/R versus dimensionless time t/τ_{VC}, for four different fluids: water (squares), 4.04% (circles) and 80.22% (triangles) methanol-water mixtures, and pure methanol (diamonds). Solid lines in Fig. 6(b) correspond to experimentally obtained curve fits for the early-stage spreading and the dashed line corresponds to the Tanner's law, $\alpha = 0.1$, observed during late-stage spreading in previous studies [53].

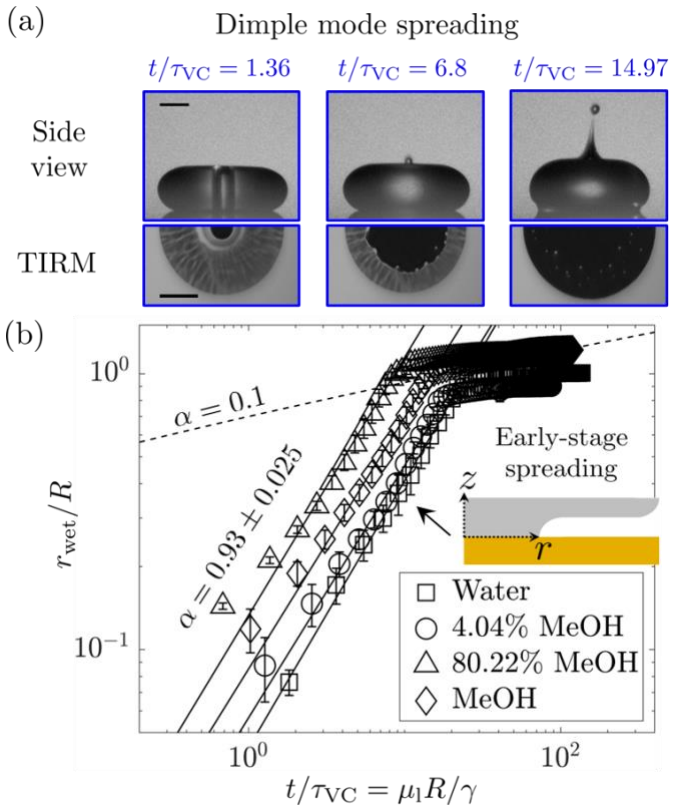

FIG. 6. Spreading dynamics of dimple mode for water (squares), 4.04% (circles) and 80.22% (triangles) methanol-water mixtures, and pure methanol (diamonds) droplets at impact We ≈ 4.9, 5.8, 9.4 and 5.5, respectively. (a) The synchronized side view and TIRM images show 80.22% methanol-water mixtures at dimensionless times $t/\tau_{VC} = 1.36$, 6.8, and 14.97 for dimple mode spreading, where $\tau_{VC} = \mu_l R/\gamma$ is the visco-capillary timescale. Scalebars represent 0.5 mm. (b) A log-log scale plot of dimensionless spreading radius r_{wet}/R versus dimensionless time t/τ_{VC} for dimple mode spreading, for various fluids. The error bars represent standard deviation of the wetting radius at each time frame. Schematic in inset of (b) shows the typical spreading front shape during early-stage spreading. Experimentally, the dimple mode exhibited an early-stage spreading dynamics of $r_{wet}/R \sim (t/\tau_{VC})^{\alpha}$, where $\alpha = 0.93 \approx 1$ was obtained, as shown using solid lines. The visco-capillary timescale is of the order $\tau_{VC} \sim \mathcal{O}(10^{-5})$s for all the droplet impact cases considered herein. The dashed line corresponds to the Tanner's law ($\alpha = 0.1$) observed during late-stage spreading.

As shown in Fig. 6(b), for the droplets exhibiting the dimple contact mode, the dimensionless spreading radius versus dimensionless time exhibited an early-stage spreading dynamics of $r_{wet}/R \sim (t/\tau_{VC})^{\alpha}$, where $\alpha = 0.93 \approx 1$ was obtained. The solid lines were plotted by curve fitting the experimental early-stage spreading data to the dimensionless expression shown above. The measured spreading rate exponent, $\alpha \approx 1$, was similar to the ones reported for early-stage

visco-capillary coalescence of two droplets [53,61–66]. Additionally, neither the impact condition nor the liquid properties had any significant effect on the spreading rate, as seen from the We values and the surface tension values of the droplet. As mentioned in the introduction, the drop coalescence phenomenon follows the visco-capillary scaling at early times and then transitions to the inertio-capillary scaling, where the former and latter regimes exhibit spreading exponent of 1 and 0.5, respectively. However, for the dimple mode spreading, the spreading rate follows $r_{wet}/R \sim t/\tau_{\mathrm{VC}}$ over the entire duration of early-stage spreading and does not exhibit any transition. Additionally, in Fig. 6(b), we also plot $\alpha = 0.1$ for the Tanner's law (dashed line), where the experimental data for late-stage spreading shows exponents similar to $\alpha = 0.1$ [53].

Here we compare the dimple mode spreading and coalescing droplets. In droplet coalescence, we assume that the drop remains nearly spherical at early times and the spreading is axisymmetric and a liquid bridge forms between the two droplets. In Fig. 7(a), we show the schematic of the initial neck shape for drop coalescence. The liquid bridge has a radius r_{wet} and a height ζ, where $\zeta \to 0$ as $r_{\mathrm{wet}} \to 0$ which gives rise to a large capillary driving force. For early times ($\sim \mathcal{O}(10^{-6} - 10^{-5})$s), the liquid bridge remains under a nearly spherical droplet (for small ζ) and at later times, the spherical shape of the droplet is lost when the meniscus height ζ becomes larger than the viscous length scale $l_v \equiv {\mu_{\mathrm{l}}}^2/\rho_{\mathrm{l}}\gamma$ and hence the spreading transitions from the visco-capillary regime to the inertio-capillary regime [53,58,61–66]. Additionally, the visco-capillary scaling can also be observed when the viscosity of the fluid surrounding the droplet is increased, thus slowing down the contact initiation and subsequent spreading [59,60].

For the case of dimple mode, the droplet deforms significantly during the pre-impact stage creating a flatter bottom characterized by a thin layer of air between the droplet and the surface. When the droplet-surface contact is initiated at the central axis, a tiny liquid bridge is formed with

radius r_{wet}, whose height ζ is of the order of air film height $\sim \mathcal{O}(10^1 - 10^2)$ nm. Here, the minimum r_{wet} that can be measured depends on the spatial resolution of the TIRM images (~5 μm), which is at least two orders of magnitude larger than the air film height ahead of the neck. The curvature of the air-liquid meniscus following $\kappa \sim \mathcal{O}(1/h_{\text{air}})$ (since $h_{\text{air}} \ll r_{\text{wet}}$) drives the liquid into the bridge from the droplet above it and leads to an increase in r_{wet} with time. Unlike drop coalescence where the curvature κ decreases with time (i.e., ζ increases with time, as shown in Fig. 7(a)), the curvature κ in dimple mode spreading remains relatively constant over time (i.e., ζ is sustained, as shown in Figs. 7(b)-(c)), due to the presence of the thin air film ahead of the spreading front. The sustained meniscus of height $\zeta \sim h_{\text{air}}$ during early-stage spreading leads to a balance between the capillary driving force and the viscous dissipation force and hence a constant spreading rate of $\alpha \approx 1$ is observed for the dimple mode spreading shown in Fig. 6(b). Additionally, we can also see from the TIRM view in Fig. 6(a) (rightmost panel) that once the droplet has spread significantly and the air film vanishes, the spreading rate decreases significantly as shown in Fig. 6(b) for $t/\tau_{\text{VC}} > 10^1$, where thin air film ceases to exist and the Tanner's law governs the spreading dynamics [53]. The visco-capillary spreading regime observed for the dimple mode occurs due to the presence of a thin air film of height $\zeta \sim h_{\text{air}}$ during the entire duration of early-stage spreading of a deformed droplet. While the maximum contact line speed is presumably at the instant of contact at the center of the droplet, the surface bubbles are entrapped only during the constant spreading rate regime due to the amount of time required for the air pressure buildup near the contact line [48]. The geometry of the air film is also crucial for the entrapment to occur, which was also found to be the reason for failure in coating flows [11].

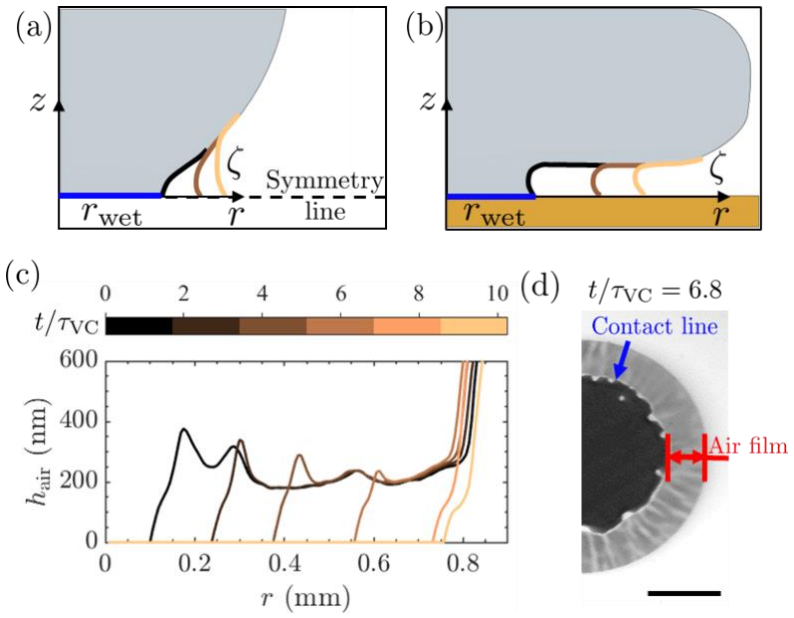

FIG. 7. Schematic of meniscus shape close to the contact line for (a) drop coalescence and (b) dimple mode spreading. The meniscus height ζ increases with time for drop coalescence and ζ remains relatively constant over the spreading duration for dimple mode spreading. (c) Post-contact air film profile h_{air} ahead of the wetting front over the spreading period for the 80.22% methanol-water mixtures drop impact shown in Fig. 6. The colormap in (c) represents the dimensionless time of spreading t/τ_{VC}. (d) TIRM image at t/τ_{VC} =6.8 corresponding to the case in (c), where the blue and red arrows indicate the contact line and air film respectively. The scale bar in (d) represents 0.5 mm.

It is important to note that, the TIRM technique presented here enables accurate probing of early-stage post-contact spreading dynamics of drop impact, which has been difficult from side-view images. In addition, most prior droplet impact studies focus on high impact velocities where the droplet-surface contact occurs off-centered (non-axisymmetric) and the spreading rate measurements for such contacts can be challenging. The film contact mode (see Fig. 3(a)) occurs at random locations within the thin air film region and existing scaling models are not applicable for such non-axisymmetric spreading cases. Using the dimple contact mode reported herein, an axisymmetric droplet-surface contact can be initiated, and the axisymmetric spreading front propagation can be successfully used to study the spreading speed.

4. Critical capillary number for bubble entrapment

The TIRM panels in Fig. 5 show that radial bubbles were entrapped during the early-stage dimple contact spreading. An unstable contact line can be observed at t/τ_{VC} =6.8 in the TIRM image (Fig. 6(a)). The wetting failure was observed during the early-stage spreading dynamics, $r_{\mathrm{wet}}/R \sim (t/\tau_{\mathrm{VC}})^1$, resulting in radial bubble entrapment. The observation above motivated us to investigate capillary number, $\mathrm{Ca} = U_{\mathrm{wet}}\mu_{\mathrm{l}}/\gamma$, for the wetting process, where the $U_{\mathrm{wet}} = dr_{\mathrm{wet}}/dt$ is the contact line velocity, and its implication on the critical capillary number for bubble entrapment.

Wetting failure for coating flows has been well studied both theoretically [77–79] and experimentally [11,80]. The critical capillary number for wetting failure, predicted by the asymptotic analysis, scales as [11]

$$\mathrm{Ca}^{\mathrm{crit}} \sim \frac{\pi|\ln\lambda|}{6} - \frac{\theta_{\mathrm{mic}}^3}{9} \tag{1}$$

where $\lambda = \mu_{\mathrm{g}}/\mu_{\mathrm{l}}$ is the viscosity ratio of air and spreading liquid, and θ_{mic} is the microscopic contact angle. The assumption and derivation for Eq. (1) is included in Section S.6 of the Supplemental Materials [83]. For a system where liquid displaces air, the viscosity ratio always falls in the range $0 < \lambda \ll 1$. When the liquid viscosity increases, the absolute value of the logarithmic term in Eq. (1) increases, implying a higher $\mathrm{Ca}^{\mathrm{crit}}$ threshold for wetting failure. However, the $\mathrm{Ca}^{\mathrm{crit}}$ decreases with an increase in microscopic angle θ_{mic}, which implies that a more wettable surface increases the threshold contact line speed, U_{wet}, for wetting failure. Using Eq. (1) and assuming that the wetting failure is a precursor to the bubble entrapment and the critical capillary numbers of the wetting failure for fluids baseline and 2 are of the same order, we get

$$\mathrm{Ca}_2^{\mathrm{bubble}} \approx \frac{\mathrm{Ca}_2^{\mathrm{crit}}}{\mathrm{Ca}_{\mathrm{base}}^{\mathrm{crit}}}.\mathrm{Ca}_{\mathrm{base}}^{\mathrm{bubble}} \approx \frac{3\pi|\ln\lambda_2| - 2\theta_{\mathrm{mic},2}^3}{3\pi|\ln\lambda_{\mathrm{base}}| - 2\theta_{\mathrm{mic,base}}^3}.\mathrm{Ca}_{\mathrm{base}}^{\mathrm{bubble}} \tag{2}$$

where the superscripts crit and bubble represent the critical values of wetting failure and bubble entrapment, respectively. Equation (2) can be used to estimate the bubble entrapment of a new fluid drop based on the fluid properties and the critical capillary number of bubble entrapment for a baseline fluid.

Consider a water droplet as the baseline case, the critical capillary numbers for bubble entrapment for pure methanol and methanol-water mixtures can be estimated using Eq. (2). Here, the experimentally determined critical capillary number of bubble entrapment for a water droplet is $\mathrm{Ca}_{\mathrm{base}}^{\mathrm{bubble}} = 0.048$, corresponding to $\mathrm{We} = 4.4$, with detailed described in the Supplemental Material [83]. Using the interfacial tension for silicone oil-gas, γ_{sg}, shown in Table I and for silicone oil-liquid, γ_{sl}, measured using an in-house pendant drop tensiometry method [81,82], θ_{mic} can be determined following $\cos(\theta_{\mathrm{mic}}) = (\gamma_{\mathrm{sg}} - \gamma_{\mathrm{sl}})/\gamma$.

Figure 8 shows the TIRM images (left panels) at different dimensionless times for (a) 4.04% and (b) 80.22% methanol-water mixture droplets, and (c) pure methanol droplet and the experimentally measured Ca versus dimensionless time (right panels). As seen from TIRM images of Fig. 8(a) and (b), the 4.04% and 80.22% methanol-water mixture droplets undergoing dimple mode spreading entrapped radial bubbles (blue ellipse). However, for the pure methanol droplet shown in Fig. 8(c), all bubbles were suppressed. To determine how the Ca value compares with the critical capillary number for bubble entrapment predicted from theory, we plot the experimentally measured Ca (symbols) versus dimensionless time against Eq. (2) (dashed lines) for bubble entrapment. For the 4.04% and 80.22% methanol-water mixture droplets where the radial bubble entrapment occurred (Figs. 8(a) and (b) left panels), the Ca value was above the critical capillary number for bubble entrapment (Figs. 8(a) and (b) right panels). However, for the pure methanol droplet where all radial bubbles were suppressed (Fig. 8(c) left panel), the Ca value

never exceeded the critical capillary number for bubble entrapment (Fig. 8(c) right panel). The calculated critical capillary number, $\mathrm{Ca}^{\mathrm{bubble}}$, for 4.04% and 80.22% methanol-water mixtures, and pure methanol were 0.049, 0.068 and 0.06, respectively, based on Eq. (2).

Regardless of the difference in fluid surface tensions, a thin air film ahead of the contact line (red arrows) can be observed from the TIRM images in Fig. 8, when the drop initially spreads on the surface. As mentioned in Sec. III. B. 3., the high curvature due to air film geometry is responsible for the high capillary number during the early spreading stage. As the spreading radius increases, the air film is no longer present ahead of the contact line, which leads to decrease in the spreading rate, and hence a decrease in capillary number is seen in Figs. 8 (a-c) right panels. This observation confirms the fast-spreading dynamics, $r_{\mathrm{wet}}/R \sim (t/\tau_{\mathrm{VC}})^1$ at early-stage is due to the high capillary driving force of the air film geometry. From the TIRM images, we can also observe that the number and size of radial entrapped bubbles decreases as the methanol concentration increases, suggesting that a decrease in liquid-gas surface tension not only increases the threshold for bubble entrapment, $\mathrm{Ca}^{\mathrm{bubble}}$, but may also decrease the number and size of entrapped radial bubbles. Based on the above observations, the critical capillary number calculated using Eq. (2) can be used to reasonably predict when the bubble entrapment would occur for a given liquid, provided the experimentally measured capillary number for bubble entrapment for a base fluid is accurately measured. Overall, the results suggest that reduction in liquid surface tension for droplets spreading via dimple mode can lead to suppression of all surface bubbles and improved droplet deposition.

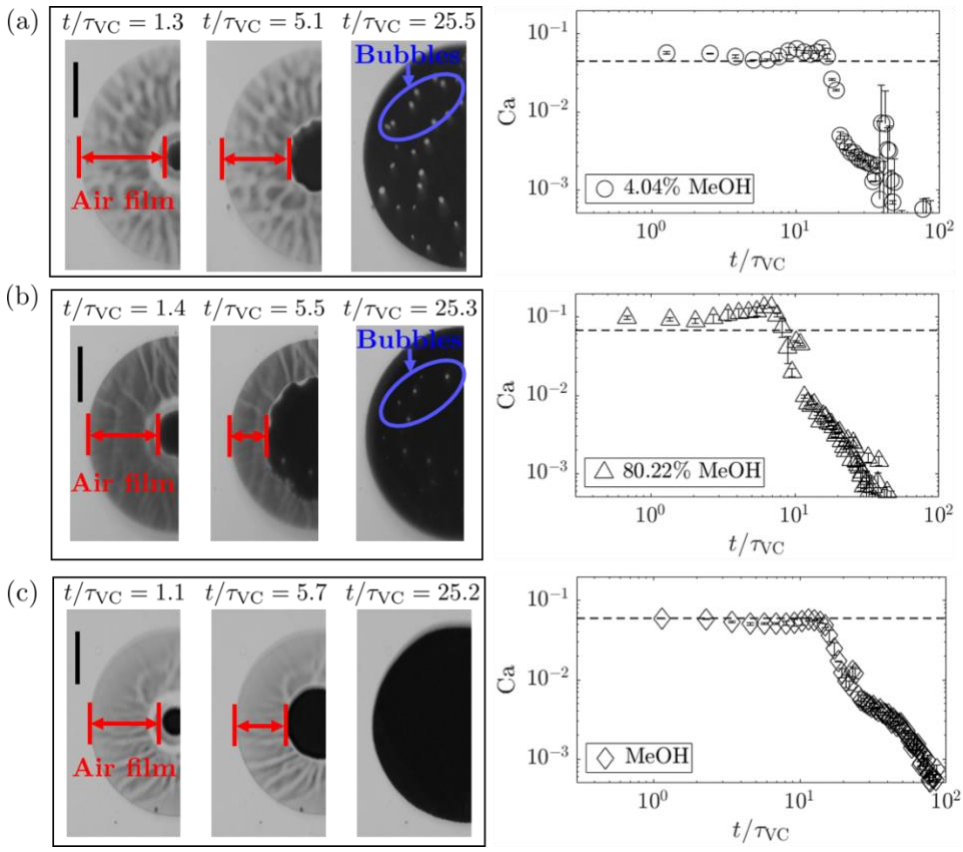

FIG. 8. The left panels show the TIRM views at different dimensionless times for (a) 4.04%, (b) 80.22% methanol-mixture droplets, and (c) pure methanol droplets at impact We ≈ 5.8, 9.4 and 5.5, respectively. Bubble entrapment (blue ellipse) was observed for (a) and (b), while all bubbles were suppressed for (c). The extended air film ahead of the contact line is denoted using the red arrow. The right panels show the experimentally measured capillary number, $\mathrm{Ca} = \mu_l U_{wet}/\gamma$, versus the dimensionless time, t/τ_{VC}, corresponding to the cases shown in the left panel. The symbols represent the experimentally measured value, and the dashed lines represent the estimated critical capillary number for bubble entrapment using Eq. (2). At each time frame, the error bars represent standard deviation of Ca due to variation of wetting speed at different azimuthal position. During the early stage spreading, for (a) 4.04% and (b) 80.22% methanol-water mixture droplets, where bubble entrapment was observed, the value of Ca is higher than the critical capillary number predicted for bubble entrapment, while for the pure methanol droplet, where all bubbles were suppressed, the value of Ca never exceeds the critical capillary number predicted for bubble entrapment. For dimensionless times larger than 10^1, the value of Ca suddenly decreases, as spreading transitions from early-stage to viscosity denominated regime.

IV. CONCLUSION

Droplet impact experiments were performed on a lubricated smooth surface at low and intermediate impact Weber numbers (We $\sim \mathcal{O}(10^0 - 10^1)$) to elucidate dimple contact mode,

where droplet-surface contact is initiated at the droplet's central axis and film mode contact, where droplet-surface contact is initiated randomly at the thinnest region of the air film. The post-contact bubble entrapment scenarios were systematically studied, and the dimple contact mode was found to suppress the surface central bubble. Entrapment of surface bubbles were suppressed by reducing the impact velocity. The effect of droplet's viscosity and surface tension on bubble entrapment were also studied independently, where the increase in droplet viscosity led to droplet bounce-off and the decrease in surface tension led to reduction in surface bubble size. The contact line propagation speed was found to decrease when the droplet's surface tension was reduced. At higher We, the droplet-surface contact occurs at the thinnest region of the air film via film mode of contact which always entraps both central and radial bubbles.

The early-stage post-contact spreading dynamics was then examined for dimple mode of contact, which exhibits the visco-capillary scaling of $\alpha \approx 1$, independent of both the impact conditions and the drop surface tension. Late-stage spreading was found to follow the well-known Tanner's law. A critical capillary number, calculated based on wetting failure and bubble entrapment of a water droplet, was used to predict the bubble entrapment conditions for a given liquid with good accuracy, providing valuable insight into bubble suppression strategies.

ACKNOWLEDGEMENTS

Support for this work was provided by the US National Science Foundation under Grant No. CBET-1705745.

Reference

[1] P. A. Schweitzer, *Paint and Coatings: Applications and Corrosion Resistance* (CRC press, 2005).

[2] A. Dalili, S. Chandra, J. Mostaghimi, H. T. C. Fan, and J. C. Simmer, *Bubble Entrapment and Escape from Sprayed Paint Films*, Prog. Org. Coatings **97**, 153 (2016).

[3] D. B. van Dam and C. Le Clerc, *Experimental Study of the Impact of an Ink-Jet Printed Droplet on a Solid Substrate*, Phys. Fluids **16**, 3403 (2004).

[4] D. Lohse, *Fundamental Fluid Dynamics Challenges in Inkjet Printing*, Annu. Rev. Fluid Mech. **54**, 349 (2022).

[5] X. Dong, H. Zhu, and X. Yang, *Characterization of Droplet Impact and Deposit Formation on Leaf Surfaces*, Pest Manag. Sci. **71 (2)**, 302 (2015).

[6] M. Damak, S. R. Mahmoudi, M. N. Hyder, and K. K. Varanasi, *Enhancing Droplet Deposition through In-Situ Precipitation*, Nat. Commun. **7**, 12560 (2016).

[7] W. Jia and H. H. Qiu, *Experimental Investigation of Droplet Dynamics and Heat Transfer in Spray Cooling*, Exp. Therm. Fluid Sci. **27**, 829 (2003).

[8] A. L. N. Moreira, A. S. Moita, and M. R. Panão, *Advances and Challenges in Explaining Fuel Spray Impingement: How Much of Single Droplet Impact Research Is Useful?*, Prog. Energy Combust. Sci. **36**, 554 (2010).

[9] D. Attinger, C. Moore, A. Donaldson, A. Jafari, and H. A. Stone, *Fluid Dynamics Topics in Bloodstain Pattern Analysis: Comparative Review and Research Opportunities*, Forensic Sci. Int. **231**, 375 (2013).

[10] N. Laan, K. G. De Bruin, D. Slenter, J. Wilhelm, M. Jermy, and D. Bonn, *Bloodstain Pattern Analysis: Implementation of a Fluid Dynamic Model for Position Determination of Victims*, Sci. Rep. **5**, 11461 (2015).

[11] E. Vandre, M. S. Carvalho, and S. Kumar, *On the Mechanism of Wetting Failure during Fluid Displacement along a Moving Substrate*, Phys. Fluids **25**, 102103 (2013).

[12] S. T. Thoroddsen, T. G. Etoh, and K. Takehara, *Air Entrapment under an Impacting Drop*, J. Fluid Mech. **478**, 125 (2003).

[13] S. T. Thoroddsen, T. G. Etoh, K. Takehara, N. Ootsuka, and Y. Hatsuki, *The Air Bubble Entrapped under a Drop Impacting on a Solid Surface*, J. Fluid Mech. **545**, 203 (2005).

[14] S. T. Thoroddsen, T. G. Etoh, and K. Takehara, *High-Speed Imaging of Drops and Bubbles*, Annu. Rev. Fluid Mech. **40**, 257 (2008).

[15] C. Josserand and S. T. Thoroddsen, *Drop Impact on a Solid Surface*, Annu. Rev. Fluid Mech. **48**, 365 (2016).

[16] L. Chen, L. Li, Z. Li, and K. Zhang, *Submillimeter-Sized Bubble Entrapment and a High-Speed Jet Emission during Droplet Impact on Solid Surfaces*, Langmuir **33**, 7225 (2017).

[17] Y. L. Hung, M. J. Wang, J. W. Huang, and S. Y. Lin, *A Study on the Impact Velocity and Drop Size for the Occurrence of Entrapped Air Bubbles - Water on Parafilm*, Exp. Therm. Fluid Sci. **48**, 102 (2013).

[18] P. G. Pittoni, Y. C. Lin, R. J. Wang, T. S. Yu, and S. Y. Lin, *Bubbles Entrapment for Drops Impinging on Polymer Surfaces: The Roughness Effect*, Exp. Therm. Fluid Sci. **62**, 183 (2015).

[19] S. Mitra, Q. Vo, and T. Tran, *Bouncing-to-Wetting Transition for Droplet Impact on Soft Solids*, Soft Matter **17**, 5969 (2021).

[20] E. Q. Li, I. U. Vakarelski, and S. T. Thoroddsen, *Probing the Nanoscale: The First Contact of an Impacting Drop*, J. Fluid Mech. **785**, R2 (2015).

[21] K. R. Langley, E. Q. Li, I. U. Vakarelski, and S. T. Thoroddsen, *The Air Entrapment under a Drop Impacting on a Nano-Rough Surface*, Soft Matter **14**, 7586 (2018).

[22] V. Mehdi-Nejad, J. Mostaghimi, and S. Chandra, *Air Bubble Entrapment under an Impacting Droplet*, Phys. Fluids **15**, 173 (2003).

[23] P. D. Hicks and R. Purvis, *Air Cushioning and Bubble Entrapment in Three-Dimensional Droplet Impacts*, J. Fluid Mech. **649**, 135 (2010).

[24] J. S. Lee, B. M. Weon, J. H. Je, and K. Fezzaa, *How Does an Air Film Evolve into a Bubble during Drop Impact?*, Phys. Rev. Lett. **109**, 204501 (2012).

[25] S. T. Thoroddsen, K. Takehara, and T. G. Etoh, *Bubble Entrapment through Topological Change*, Phys. Fluids **22**, 051701 (2010).

[26] K. R. Langley and S. T. Thoroddsen, *Gliding on a Layer of Air: Impact of a Large-Viscosity Drop on a Liquid Film*, J. Fluid Mech. **878**, R2 (2019).

[27] K. Langley, E. Q. Li, and S. T. Thoroddsen, *Impact of Ultra-Viscous Drops: Air-Film Gliding and Extreme Wetting*, J. Fluid Mech. **813**, 647 (2017).

[28] J. Palacios, J. Hernández, P. Gómez, C. Zanzi, and J. López, *On the Impact of Viscous Drops onto Dry Smooth Surfaces*, Exp. Fluids **52**, 1449 (2012).

[29] M. M. Driscoll and S. R. Nagel, *Ultrafast Interference Imaging of Air in Splashing Dynamics*, Phys. Rev. Lett. **107**, 154502 (2011).

[30] X. Tang, A. Saha, C. K. Law, and C. Sun, *Bouncing-to-Merging Transition in Drop Impact on Liquid Film: Role of Liquid Viscosity*, Langmuir **34**, 2654 (2018).

[31] X. Tang, A. Saha, C. Sun, and C. K. Law, *Spreading and Oscillation Dynamics of Drop Impacting Liquid Film*, J. Fluid Mech. **881**, 859 (2019).

[32] X. Tang, A. Saha, C. K. Law, and C. Sun, *Bouncing Drop on Liquid Film: Dynamics of Interfacial Gas Layer*, Phys. Fluids **31**, 013304 (2019).

[33] M. Pack, H. Hu, D. Kim, Z. Zheng, H. A. Stone, and Y. Sun, *Failure Mechanisms of Air Entrainment in Drop Impact on Lubricated Surfaces*, Soft Matter **13**, 2402 (2017).

[34] L. Zhang, T. Soori, A. Rokoni, A. Kaminski, and Y. Sun, *Thin Film Instability Driven*

Dimple Mode of Air Film Failure during Drop Impact on Smooth Surfaces, Phys. Rev. Fluids **6**, 044002 (2021).

[35] D. Beilharz, A. Guyon, E. Q. Li, M. J. Thoraval, and S. T. Thoroddsen, *Antibubbles and Fine Cylindrical Sheets of Air*, J. Fluid Mech. **779**, 87 (2015).

[36] U. Jain, M. Jalaal, D. Lohse, and D. Van Der Meer, *Deep Pool Water-Impacts of Viscous Oil Droplets*, Soft Matter **15**, 4629 (2019).

[37] Z. Jian, M. A. Channa, A. Kherbeche, H. Chizari, S. T. Thoroddsen, and M.-J. J. Thoraval, *To Split or Not to Split: Dynamics of an Air Disk Formed under a Drop Impacting on a Pool*, Phys. Rev. Lett. **124**, 184501 (2020).

[38] J. S. Lee, B. M. Weon, S. J. Park, J. T. Kim, J. Pyo, K. Fezzaa, and J. H. Je, *Air Evolution during Drop Impact on Liquid Pool*, Sci. Rep. **10**, 5790 (2020).

[39] H. Lhuissier, C. Sun, A. Prosperetti, and D. Lohse, *Drop Fragmentation at Impact onto a Bath of an Immiscible Liquid*, Phys. Rev. Lett. **110**, 264503 (2013).

[40] N. O. Hasan and A. Prosperetti, *Bubble Entrainment by the Impact of Drops on Liquid Surfaces*, J. Fluid Mech. **219**, 143 (1990).

[41] S. T. Thoroddsen, M. J. Thoraval, K. Takehara, and T. G. Etoh, *Micro-Bubble Morphologies Following Drop Impacts onto a Pool Surface*, J. Fluid Mech. **708**, 469 (2012).

[42] S. T. Thoroddsen, K. Takehara, H. D. Nguyen, and T. G. Etoh, *Singular Jets during the Collapse of Drop-Impact Craters*, J. Fluid Mech. **848**, R3 (2018).

[43] T. Tran, H. De Maleprade, C. Sun, and D. Lohse, *Air Entrainment during Impact of Droplets on Liquid Surfaces*, J. Fluid Mech. **726**, R3 (2013).

[44] Z. Q. Yang, Y. S. Tian, and S. T. Thoroddsen, *Multitude of Dimple Shapes Can Produce Singular Jets during the Collapse of Immiscible Drop-Impact Craters*, J. Fluid Mech. **904**, A19 (2020).

[45] L. Chen, J. Wu, Z. Li, and S. Yao, *Evolution of Entrapped Air under Bouncing Droplets on Viscoelastic Surfaces*, Colloids Surfaces A Physicochem. Eng. Asp. **384**, 726 (2011).

[46] D. Bartolo, C. Josserand, and D. Bonn, *Singular Jets and Bubbles in Drop Impact*, Phys. Rev. Lett. **96**, 1 (2006).

[47] W. Bouwhuis, R. C. A. Van Der Veen, T. Tran, D. L. Keij, K. G. Winkels, I. R. Peters, D. Van Der Meer, C. Sun, J. H. Snoeijer, and D. Lohse, *Maximal Air Bubble Entrainment at Liquid-Drop Impact*, Phys. Rev. Lett. **109**, 2 (2012).

[48] M. Pack, P. Kaneelil, H. Kim, and Y. Sun, *Contact Line Instability Caused by Air Rim Formation under Nonsplashing Droplets*, Langmuir **34**, 4962 (2018).

[49] R. Rioboo, M. Marengo, and C. Tropea, *Time Evolution of Liquid Drop Impact onto Solid, Dry Surfaces*, Exp. Fluids **33**, 112 (2002).

[50] A. L. Yarin, *Drop Impact Dynamics: Splashing, Spreading, Receding, Bouncing…*, Annu.

Rev. Fluid Mech. **38**, 159 (2006).

[51] T. C. De Goede, K. G. De Bruin, N. Shahidzadeh, and D. Bonn, *Predicting the Maximum Spreading of a Liquid Drop Impacting on a Solid Surface: Effect of Surface Tension and Entrapped Air Layer*, Phys. Rev. Fluids **4**, 053602 (2019).

[52] A. L. Biance, C. Clanet, and D. Quéré, *First Steps in the Spreading of a Liquid Droplet*, Phys. Rev. E **69**, 016301 (2004).

[53] M.-A. Fardin, M. Hautefeuille, and V. Sharma, *Spreading, Pinching, and Coalescence: The Ohnesorge Units*, Soft Matter **18**, 3291 (2021).

[54] J. C. Bird, S. Mandre, and H. A. Stone, *Short-Time Dynamics of Partial Wetting*, Phys. Rev. Lett. **100**, 234501 (2008).

[55] L. Courbin, J. C. Bird, M. Reyssat, and H. A. Stone, *Dynamics of Wetting: From Inertial Spreading to Viscous Imbibition*, J. Phys. Condens. Matter **21**, 464127 (2009).

[56] L. Chen, G. K. Auernhammer, and E. Bonaccurso, *Short Time Wetting Dynamics on Soft Surfaces*, Soft Matter **7**, 9084 (2011).

[57] L. Chen and E. Bonaccurso, *Effects of Surface Wettability and Liquid Viscosity on the Dynamic Wetting of Individual Drops*, Phys. Rev. E **90**, 022401 (2014).

[58] A. Eddi, K. G. Winkels, and J. H. Snoeijer, *Short Time Dynamics of Viscous Drop Spreading*, Phys. Fluids **25**, 013102 (2013).

[59] S. Mitra and S. K. Mitra, *Understanding the Early Regime of Drop Spreading*, Langmuir **32**, 8843 (2016).

[60] P. Bazazi, A. Sanati-Nezhad, and S. H. Hejazi, *Wetting Dynamics in Two-Liquid Systems: Effect of the Surrounding Phase Viscosity*, Phys. Rev. E **97**, 063104 (2018).

[61] D. G. A. L. Aarts, H. N. W. Lekkerkerker, H. Guo, G. H. Wegdam, and D. Bonn, *Hydrodynamics of Droplet Coalescence*, Phys. Rev. Lett. **95**, 164503 (2005).

[62] K. Fezzaa and Y. Wang, *Ultrafast X-Ray Phase-Contrast Imaging of the Initial Coalescence Phase of Two Water Droplets*, Phys. Rev. Lett. **100**, 104501 (2008).

[63] J. D. Paulsen, R. Carmigniani, A. Kannan, J. C. Burton, and S. R. Nagel, *Coalescence of Bubbles and Drops in an Outer Fluid*, Nat. Commun. **5**, 3182 (2014).

[64] J. D. Paulsen, J. C. Burton, and S. R. Nagel, *Viscous to Inertial Crossover in Liquid Drop Coalescence*, Phys. Rev. Lett. **106**, 114501 (2011).

[65] S. T. Thoroddsen, K. Takehara, and T. G. Etoh, *The Coalescence Speed of a Pendent and a Sessile Drop*, J. Fluid Mech. **527**, 85 (2005).

[66] M. Wu, T. Cubaud, and C. M. Ho, *Scaling Law in Liquid Drop Coalescence Driven by Surface Tension*, Phys. Fluids **16**, L51 (2004).

[67] J. M. Kolinski, S. M. Rubinstein, S. Mandre, M. P. Brenner, D. A. Weitz, and L. Mahadevan, *Skating on a Film of Air: Drops Impacting on a Surface*, Phys. Rev. Lett. **108**, 074503 (2012).

[68] M. Shirota, M. A. J. van Limbeek, D. Lohse, and C. Sun, *Measuring Thin Films Using Quantitative Frustrated Total Internal Reflection (FTIR)*, Eur. Phys. J. E **40**, 54 (2017).

[69] J. M. Kolinski, L. Mahadevan, and S. M. Rubinstein, *Lift-off Instability during the Impact of a Drop on a Solid Surface*, Phys. Rev. Lett. **112**, 134501 (2014).

[70] Clearco Products Co., *PSF - 100,000cSt Pure Silicone Fluid Product Information*, http://www.clearcoproducts.com/pdf/high-viscosity/NP-PSF-100,000cSt.pdf.

[71] X. Tang, A. Saha, C. K. Law, and C. Sun, *Nonmonotonic Response of Drop Impacting on Liquid Film: Mechanism and Scaling*, Soft Matter **12**, 4521 (2016).

[72] S. Lakshman, W. Tewes, K. Harth, J. H. Snoeijer, and D. Lohse, *Deformation and Relaxation of Viscous Thin Films under Bouncing Drops*, J. Fluid Mech. **920**, A3 (2021).

[73] J. M. Kolinski, L. Mahadevan, and S. M. Rubinstein, *Drops Can Bounce from Perfectly Hydrophilic Surfaces*, Europhys. Lett. **108**, 24001 (2014).

[74] J. de Ruiter, D. van den Ende, and F. Mugele, *Air Cushioning in Droplet Impact. II. Experimental Characterization of the Air Film Evolution*, Phys. Fluids **27**, 012105 (2015).

[75] J. De Ruiter, R. Lagraauw, D. Van Den Ende, and F. Mugele, *Wettability-Independent Bouncing on Flat Surfaces Mediated by Thin Air Films*, Nat. Phys. **11**, 48 (2015).

[76] M. V. Chubynsky, K. I. Belousov, D. A. Lockerby, and J. E. Sprittles, *Bouncing off the Walls: The Influence of Gas-Kinetic and van Der Waals Effects in Drop Impact*, Phys. Rev. Lett. **124**, 084501 (2020).

[77] R. G. Cox, *The Dynamics of the Spreading of Liquids on a Solid Surface. Part 2. Surfactants*, J. Fluid Mech. **168**, 195 (1986).

[78] O. V. Voinov, *Hydrodynamics of Wetting*, Fluid Dyn. **11**, 714 (1976).

[79] T. S. Chan, C. Kamal, J. H. Snoeijer, J. E. Sprittles, and J. Eggers, *Cox-Voinov Theory with Slip*, J. Fluid Mech. **900**, A8 (2020).

[80] A. Marchand, T. S. Chan, J. H. Snoeijer, and B. Andreotti, *Air Entrainment by Contact Lines of a Solid Plate Plunged into a Viscous Fluid*, Phys. Rev. Lett. **108**, 204501 (2012).

[81] A. R. White and T. Ward, *Pattern Search Methods for Pendant Drops: Algorithms for Rapid Determination of Surface Tension and Surfactant Transport Parameters*, Colloids Surfaces A Physicochem. Eng. Asp. **485**, 1 (2015).

[82] T. Soori, A. R. White, and T. Ward, *Immiscible Fluid Displacement in a Porous Media: Effect of Surfactants Introduced Ab Initio versus Surfactants Formed in-Situ*, J. Pet. Sci. Eng. **180**, 310 (2019).

[83] Supplemental Materials for "Post-contact droplet spreading and bubble entrapment mechanisms on a smooth surface."